Pion-proton backward elastic scattering between 30 and 90 GeV/c

W. F. Baker, D. P. Eartly, J. S. Klinger,* A. J. Lennox, and R. Rubinstein
Fermi National Accelerator Laboratory, Batavia, Illinois 60510

R. M. Kalbach,† A. E. Pifer, and P. A. Polakos‡
University of Arizona, Tucson, Arizona 85721

(Received 1 November 1982)

Backward elastic scattering of $\pi^{\pm}$ on protons has been measured for incident pion momenta between 30 and 90 GeV/c and $0 \leq -u \leq 0.5$ (GeV/c)^2. The u dependence of the cross sections is similar to that observed at lower momenta, and Regge models give acceptable fits to the data.

I. INTRODUCTION

This paper reports the final results of a Fermilab experiment designed to investigate πp elastic scattering in the range[1] $0 \leq -u \leq 0.5$ (GeV/c)^2 (or $180° \gtrsim \theta^{\pi}_{\text{c.m.s}} \gtrsim 160°$, where c.m.s. denotes center-of-mass system) for incident pion momenta P from 30 to 90 GeV/c. Preliminary results have already been reported.[2]

Experimental interest in backward elastic scattering was stimulated in 1964 when a hydrogen-bubble-chamber group at CERN reported[3] the observation of an accumulation of elastic events near $u=0$ with incident 4-GeV/c positive pions. Other experiments[4–12] followed, firmly establishing the existence of a sharp peak in the elastic cross section at $u=0$ for both π^+p and π^-p interactions with incident pion momenta from $\sim$2 to 20 GeV/c.

The data below 20 GeV/c are found to have a natural division at $\sim$5 GeV/c. Below this momentum, the differential cross section at $u=0$ varies considerably with momentum showing several peaks and dips. The correlation of the momenta at which these phenomena occur with the masses of known baryon resonances supports the idea that a major contribution to the backward cross section comes from resonance (N^* and Δ) formation in the s channel, followed by decay of the resonance back to πp. Good fits to the data are obtained[9] for the scattering amplitude being the sum of a Breit-Wigner resonance amplitude and a nonresonant background, usually written in terms of a Regge amplitude.

Above 5 GeV/c, the resonance contribution subsides and up to 20 GeV/c the data show the following characteristic features:

(1) The elastic differential cross section at $u=0$ for π^+p interactions is larger than for π^-p interactions. At 6 GeV/c, the ratio π^+/π^- is $\sim$4.

(2) The momentum dependence for the differential cross section at $u=0$ falls smoothly as P^{-n} (P is the laboratory momentum in GeV/c); values of n obtained are $n=2.0$ for π^-p and $n=2.7$ for π^+p scattering.

(3) For fixed incident momentum, the dependence of the differential cross section $d\sigma/du$ on u near $u=0$ is of the form e^{Bu}.

(4) For π^+p scattering, a sharp dip in $d\sigma/du$ is observed near $-u=0.15$. No such dip is observed for π^-p scattering.

Figure 1 shows some typical data existing prior to this experiment.

Although several optical models are capable of predicting peaks in the backward hemisphere,[13,14] none can satisfactorily explain the observed differences in magnitude and shape between π^+p and π^-p backward scattering. The best fits to the data were obtained with a model based on Reggeized baryon exchange.[15,16]

Typical baryon-exchange diagrams for πp backward elastic scattering are shown in Fig. 2. The scattering amplitude M for such a process in the

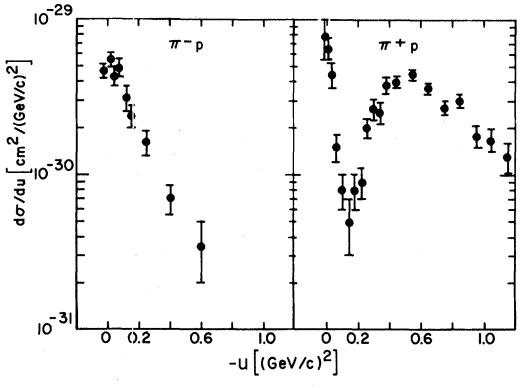

FIG. 1. Pion-proton backward elastic scattering at 7.0 GeV/c; data from Baker *et al.* (Ref. 8).

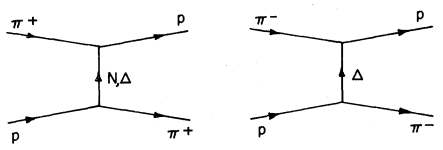

FIG. 2. Baryon-exchange diagrams for pion-proton backward elastic scattering.

Regge theory is written as[17]

$$M = F(u)\frac{1+i\tau e^{-i\pi\alpha(u)}}{\cos\pi\alpha(u)}\left[\frac{s}{s_0}\right]^{\alpha(u)-1/2},$$

where $F(u)$ is a real function of u, $\alpha(u)$ is a Regge trajectory, $\tau=\pm 1$ is the signature of the trajectory, s is the total energy in the c.m.s., and s_0 is a constant. This gives a differential cross section of the form

$$d\sigma/du \sim \frac{|M|^2}{s} = f(u)\left[\frac{s}{s_0}\right]^{2\alpha(u)-2}.$$

This expression leads to the prediction that $d\sigma/du$ for fixed u varies as a power of s; at high energies s is proportional to P so that $d\sigma/du$ varies as a power of P. We will make the conventional assumption of linear trajectories, i.e., $\alpha(u)=\alpha(0)+\alpha' u$. This assumption is observed to hold in the positive-u region of the Chew-Frautschi plot where the fit is to particle masses.

In general the Reggeized baryon-exchange model allows for the exchange of the N_α, N_γ, and Δ_δ trajectories in π^+p scattering and the exchange of only the Δ_δ trajectory in π^-p scattering. Experimental data indicate the dominance of the N_α trajectory in π^+p scattering. These data show the backward cross sections for π^-p (where only the Δ_δ trajectory is exchanged) to be appreciably smaller than for π^+p scattering up to the highest energies measured prior to this experiment. Since the Δ_δ contribution to the π^+p cross section is $\frac{1}{9}$ of its contribution to the π^-p cross section (due to Clebsch-Gordan coefficients), its contribution to the overall π^+p cross section is concluded to be small. The argument that the N_γ contribution is smaller than the N_α is based on the observation that in the region near $-u=0.15$ $(\mathrm{GeV}/c)^2$ where the N_α amplitude vanishes (see later), the π^+p cross section has a sharp dip. Since the N_γ amplitude is not predicted to vanish there, the small value of the cross section at the bottom of the dip should reflect an upper limit on the N_γ contribution. Also, since the N_γ trajectory lies below the N_α, as determined from the Chew-Frautschi plots, the influence of the N_γ exchange should decrease with increasing momentum relative to N_α.

One striking prediction of the Regge models is the existence of the dip in π^+p backward scattering. The signature term $1+i\tau e^{-i\pi\alpha(u)}$ for the N_α trajectory vanishes at $-u\simeq 0.15$ $(\mathrm{GeV}/c)^2$ (where $\alpha=-0.5$), and indeed the cross section becomes small at that u value, as seen in Fig. 1. No corresponding dip is predicted in π^-p, and none is observed. Fits to $\pi^\pm p$ backward scattering with N_α and Δ_δ trajectories were carried out in the late 1960's, and good agreement reached; an example is shown in Fig. 3. The trajectory parameters obtained were close to the Chew-Frautschi plot values.

Subsequent results from polarization experiments and from the reaction $\pi^-p\to n\pi^0$, which also may proceed by the exchange of N and Δ trajectories, could not be explained by this simple Regge model. More sophisticated models, incorporating additional trajectories, absorption, and cuts, were proposed to fit the data.[18–20] However, for $\pi^\pm p$ scattering near $u=0$ it was believed that the simple model would remain approximately valid, and we make comparisons later between this model and our data.

Using this simple model, an important prediction for data above 20 GeV/c can be obtained. Since the N_α trajectory lies below the Δ_δ, the N_α amplitude falls more rapidly than the Δ_δ with increasing momentum, so that at high enough momentum both scatterings should be dominated by Δ_δ exchange. This leads to the prediction that the π^+p cross section at $u=0$ should become $\sim\frac{1}{9}$ that of $d\sigma^-/du$,

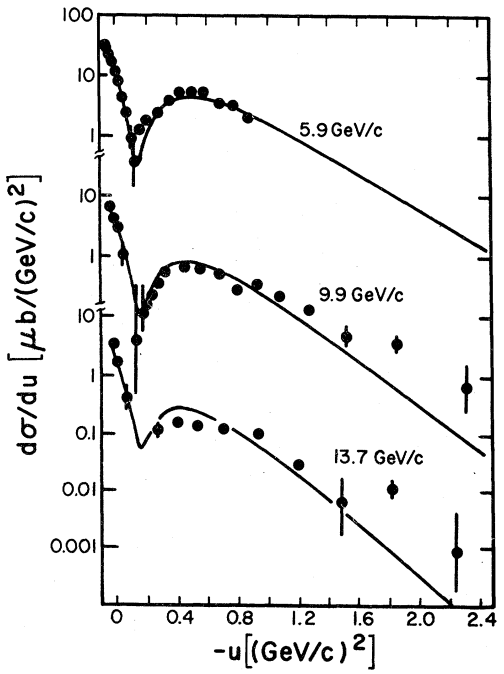

FIG. 3. Fits to the π^+p data of Owen *et al.* (Ref. 7) using the Regge model of Barger and Cline (Ref. 16).

contrary to the situation at lower momenta. The fit to low-momentum results predicts the cross sections to cross at ~ 50 GeV/c.[16,18,21] In addition, the dip in the $\pi^+ p$ angular distribution should disappear at high momentum, gradually being filled in by the contribution from the Δ_δ exchange. Eventually the π^+ angular distribution should become similar to that of π^-.

The first results above 20 GeV/c came from experiments performed at Serpukhov by Babaev *et al.*[22,23] during the first half of the 1970's, where they studied the reactions $\pi^- n \to n\pi^-$ (isotopically equivalent to $\pi^+ p \to p\pi^+$) and $\pi^- p \to p\pi^-$ at momenta near 25 and 40 GeV/c. For the former reaction, they measured $d\sigma^+/du$ at $u=0$ to be about a factor of 3 larger than was expected from an extrapolation of low momentum results using the expected $P^{-2.7}$ momentum dependence, although the angular distribution remained sharply peaked as at lower momenta. In the latter reaction, although the magnitude of the cross section $d\sigma^-/du$ at $u=0$ was consistent with Regge predictions, the angular distribution became much more peaked near $u=0$. Some data are shown in Fig. 4. These results could not be explained by the conventional Regge model. Models were proposed[24–26] which included the existence of new (non-Regge) terms in the scattering amplitude. The effect of such terms, it was argued, would not be seen at lower momenta, due to small couplings, but would have a lesser momentum dependence than Regge terms and would eventually dominate. The experiment described here was performed to test theoretical models to the highest momentum practical, and also to cover the momentum range of the Serpukhov experiments again. Its design was driven by the expectation that the cross sections to be measured would be small, of order nb/(GeV/c)^2.

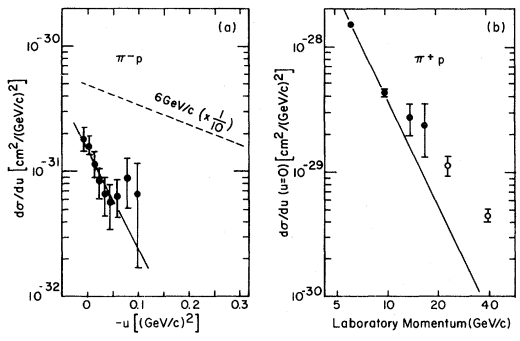

FIG. 4. (a) $\pi^- p$ data at 38 GeV/c from Babaev *et al.* (Ref. 23) together with a dashed line through the results of Owen *et al.* (Ref. 7) at 6 GeV/c. (b) $d\sigma/du$ at $u=0$ for $\pi^+ p$. Data from Owen *et al.* (Ref. 7) (below 20 GeV/c) and Babaev *et al.* (Ref. 22) (above 20 GeV/c). The line is $P^{-2.7}$.

II. EXPERIMENTAL METHOD

A. Introduction

Pions in a beam of known momentum and direction were elastically scattered off the protons in a liquid hydrogen target. The scattering angles and momenta of the recoil pions and protons were measured in separate magnetic spectrometers, each consisting of an analysis magnet with scintillation-counter hodoscopes and multiwire proportional chambers (MWPC's) on either side to determine particle trajectories. One spectrometer ("forward"), downstream of the hydrogen target, recorded the forward-scattered proton; the second ("backward") was located just upstream of the hydrogen target to record the backward-scattered pion. A threshold gas Čerenkov counter in the forward spectrometer identified the forward-scattered particle as a proton. The scintillation-counter hodoscopes provided a fast, although imprecise, momentum-angle measurement for each particle. An electronic comparison was made between the forward and backward hodoscopes, and any event whose correlation was close to that expected for an elastic scatter gave a trigger which caused the information from the MWPC's and other spectrometer instrumentation to be recorded on magnetic tape for off-line analysis. As will be described in Sec. II D, there were two different experimental layouts used for the forward spectrometer, in order to maintain resolution and acceptance over the incident momentum range from 30 to 90 GeV/c. The backward spectrometer was not changed during the experiment since the backward scattering kinematics are relatively independent of incident momentum. Figure 5 shows the experimental layout for 30 and 50 GeV/c data taking.

The experiment used beam for a total of 1500 h including setup time. A summary of the data acquired and analyzed during the experiment is given in Table I. A more detailed description of the apparatus follows.

B. Beam

This experiment used the M6 beam in the Meson Area at Fermilab. The pions were produced by a 400-GeV proton beam from the Fermilab proton synchrotron striking a $30.5 \times 0.15 \times 0.15$ cm beryllium target. Secondary particles produced at a 2.5-mrad horizontal angle were collected, momentum analyzed, and identified in a 420-m-long beam line, and directed onto the liquid hydrogen target. A schematic layout of the beam-transport components

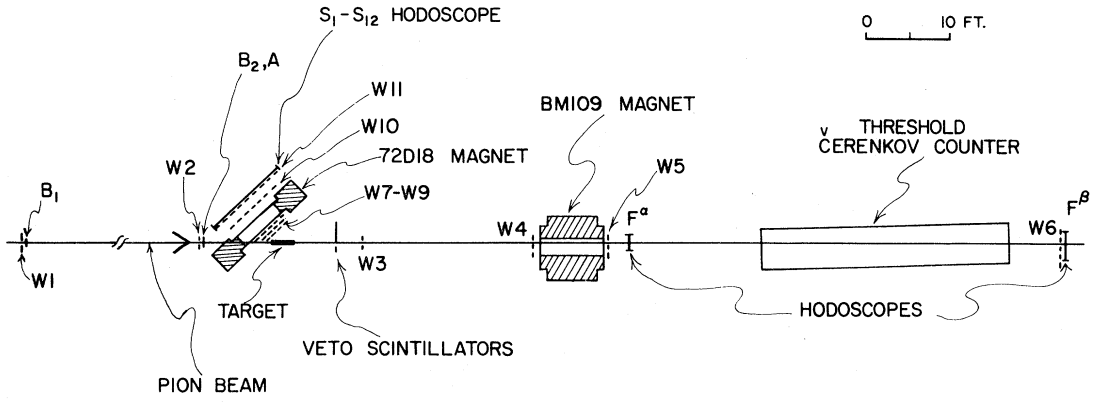

FIG. 5. Layout of the experiment for 30 and 50 GeV/c. $W1$—$W11$ represent groups of MWPC's; S_1—S_{12}, F^α, and F^β are scintillation-counter hodoscopes. B_1, B_2, and A are scintillation counters. Not shown are scintillation counters and a threshold Čerenkov counter in the incident beam upstream from the region shown in the figure.

is shown in Fig. 6, and a more complete description is available in Ref. 27.

The beam contained three stages and three foci; each stage contained the sequence: point-to-parallel quadrupoles, dipole, parallel-to-point quadrupoles. The momentum acceptance of the beam was defined by a collimator at the first focus. During the experiment its aperture was varied to maintain the desired flux on the liquid hydrogen target.

Momentum dispersion at the second focus was 4.442 cm per $(\%\,\Delta p/p)$, and a momentum-measuring scintillation-counter hodoscope was placed at this location. For this experiment, a parallel beam at the liquid hydrogen target was desired, and so the final beam quadrupoles (Q_{14}—Q_{17} in Fig. 6) were not used.

Beam particles were recorded by two scintillation counters (B_1,B_2 in Fig. 5), together with A, a halo veto counter with a hole for the beam to pass through. The dimensions of all counters are given in Table II.

Particle identification in the incident beam was provided by an 18-m-long helium-gas threshold Čerenkov counter C_π located in the third section of the beam line. With its pressure adjusted just above pion threshold, it eliminated triggers caused by protons or kaons. The remaining muons and electrons were measured at every beam momentum and polarity. The percentage of muons was determined by measuring beam transmission through a 4.5-m iron beam stop, and varied between 1% and 2% depending on beam momentum. Electrons were measured with a lead-glass shower counter, and varied from $\sim 10\%$ of the beam at 30 GeV/c to a negligible fraction above 70 GeV/c.

At the hydrogen target the beam size was approximately 3.8 cm in diameter, with a divergence of $\sim \pm 0.3$ mrad and a nominal momentum spread of $\pm 0.2\%$. There were approximately 1.5×10^6 beam pions per 1-sec synchrotron spill. The pion beam had the accelerator rf time structure, and the pions arrived in "buckets," each separated by 18.8 nsec; roughly 1 bucket in 35 was occupied by a beam particle.

A 32-element scintillation-counter hodoscope was placed at the second focus to measure the relative momentum of each incident pion. Each element was 3 mm wide and overlapped its neighbor by one

TABLE I. Summary of data taken.

Incident particle	Momentum (GeV/c)	Pions on target	Event triggers	Elastic events
π^+	30	25.5×10^9	130×10^3	100
π^+	50	45.4×10^9	263×10^3	62
π^+	70	49.6×10^9	621×10^3	14
π^-	30	33.7×10^9	256×10^3	142
π^-	50	88.6×10^9	271×10^3	121
π^-	70	58.3×10^9	305×10^3	31
π^-	90	43.0×10^9	233×10^3	13

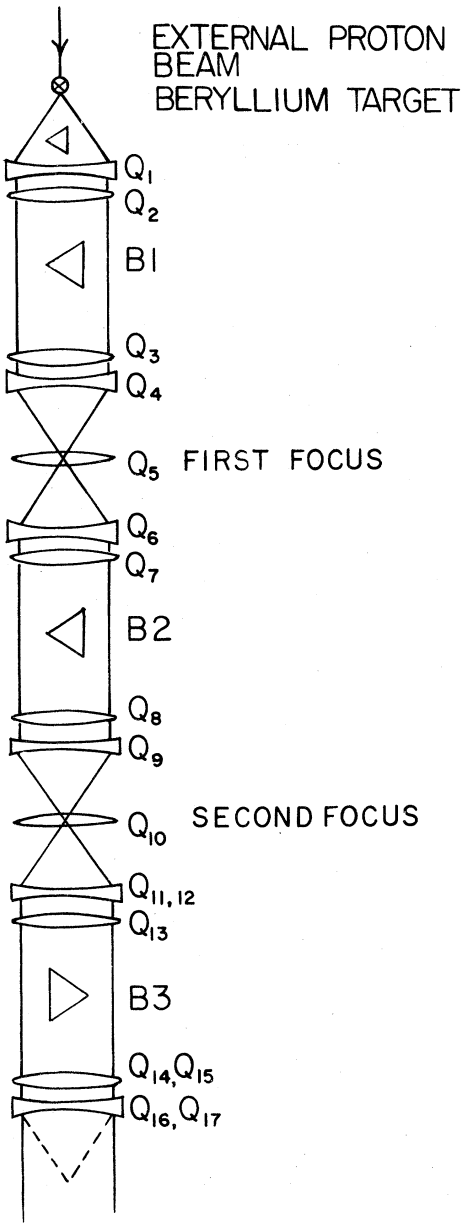

FIG. 6. Schematic arrangement of the Fermilab M6 beam.

TABLE II. Scintillation-counter dimensions, horizontal × vertical. Typical sizes for hodoscope elements are given when not all identical.

B_1, B_2	2 in. diameter circular
A	5.5 in. × 5.5 in. with 2-in.-diameter circular hole
S_i	11 in. × 12 in.
F^α	2.75 in. × 7.5 in.
F^β	9.38 in. × 14.5 in.

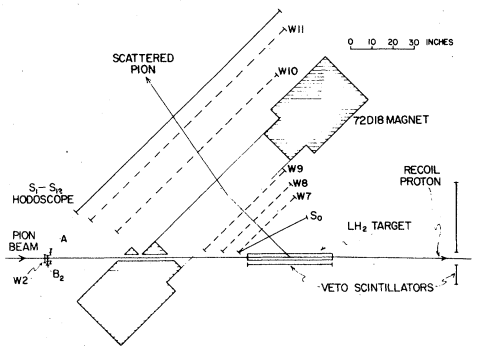

FIG. 7. Backward-spectrometer layout.

third giving a spatial resolution of 1 mm; this corresponded to a momentum resolution of ±0.024%. The absolute value of the central momentum was set by means of a nuclear magnetic resonance apparatus installed in a beam dipole. Two sets of wire proportional chambers ($W1$ and $W2$ in Figs. 5 and 7) located 22 and 3 m, respectively, upstream of the liquid hydrogen target provided directional and positional information on each incident pion. Each set contained both x and y planes with wire spacings of 2 mm.

C. Liquid hydrogen target

The target was a cylindrical vessel, 1 m along the beam direction and 7.5 cm in diameter, constructed of 0.25 mm Mylar. The vessel was wrapped in ~40 layers of 6.4 μm aluminized Mylar thermal insulation in an evacuated outer vessel. The outer vessel had a large exit window constructed of 0.4 mm Mylar spanning the entire length of one side and the upstream face, to allow for the incoming beam and the large angular range of the outgoing scattered pions. Another window at the downstream end allowed the outgoing proton and the uninteracted beam to exit from the target. The target vessel was filled with hydrogen liquified by a small helium refrigerator. During empty-target runs, the hydrogen was transferred to a reservoir above the target.

All sides of the target enclosure, excluding the windows, were covered by veto counters to improve rejection of inelastic interactions. Additional veto counters (some preceded by a thin lead sheet) were also located downstream of the target (see Figs. 5 and 7).

D. Forward spectrometer

Trajectory and momentum information on the forward-going proton was provided by four sets of MWPC's located on either side of an analysis magnet as shown in Fig. 5. The two chambers ($W3, W4$)

located between the target and the magnet consisted of one x and one y plane each; the two behind the magnet ($W5$,$W6$), one x plane each. Lateral wire spacing for all planes was 2 mm and the chamber sizes were always such that they did not constitute aperture limits. Momentum measurement was by means of either one or two standard Fermilab BM109 analysis magnets. Each magnet had a gap of 24 in.$\times$6 in. and a pole length of 72 in.

In order that resolution and acceptance could be maintained over the desired momentum range from 30 to 90 GeV/c, two experimental layouts were used. In the first (shown in Fig. 5), for data taking at $\pm$30 and $\pm$50 GeV/c, the overall spectrometer length was 30 m with a single analysis magnet located 11 m from the target; its magnetic-field integral was 1337 kG in. for both incident momenta, which provided a momentum resolution

$$\frac{\Delta P}{P^2}=\pm 2\times 10^{-4}\ (\mathrm{GeV}/c)^{-1}\ .$$

The scattering-angle resolution $\Delta\theta$ of this arrangement was $\pm$0.34 mrad.

In the second layout, used for additional running at -50 GeV/c, and for running at $\pm$70 and -90 GeV/c, the overall spectrometer length was increased to 60 m. Two analysis magnets, located a distance of 31 m from the target, were used to obtain the desired momentum resolution. Their magnetic field was scaled with momentum to provide the same resolution at each momentum, with a total field integral of 2546 kG in. at 90 GeV/c. This geometry had momentum ($\Delta P/P$) and scattering-angle resolutions of $\pm$0.4% and $\pm$0.110 mrad, respectively. For both layouts, the forward spectrometer acceptance for backward elastic scattering was well matched to that of the backward spectrometer.

The forward spectrometer contained two hodoscope planes of eight scintillation counters each, located downstream of the analysis magnet (F^α,F^β in Fig. 5) to provide some determination of the scattering angle and momentum of the forward particle. The F^α counters were placed side by side, while those of the F^β hodoscope partially overlapped. The elements of each hodoscope were located such that a simple coincidence between a given element in F^α and the corresponding element in F^β signaled a particle of scattering angle and momentum consistent with an elastic scatter. The counter sizes are given in Table II. The approximate resolution of a pair of elements was $\sim$5 and $\sim$3 mrad for the low- and high-momentum geometries, respectively, corresponding to a momentum resolution, $\Delta P/P \simeq \pm 13\%$. The information from these telescopes, together with that from the backward spectrometer hodoscope, provided the kinematic constraints in the trigger in order to heavily favor elastic scattering.

A 1.5-m-diam, 9-m-long nitrogen-gas-filled Čerenkov counter (C_F) was also located in the downstream part of the forward spectrometer. Four adjacent spherical mirrors mounted at the downstream end focused the light onto the 1.5 in. photocathode of an RCA 31000M photomultiplier. Particles leaving the counter had to traverse the 1-in.-thick mirror glass so the counter was placed as close as possible to the final MWPC to minimize position measurement errors caused by multiple Coulomb scattering and interactions in the glass. The pressure was set just below the threshold of the highest-momentum proton expected from an elastic scatter, to veto forward pions. The counter was most useful in the π^+ running, where an inelastically forward scattered π^+ often could closely resemble in kinematics the proton from a backward elastic scatter. In this case, the trigger rate was typically reduced a factor of 70 by including the Čerenkov counter in veto. For π^- running, a forward-scattered π^- was deflected in the opposite direction by the analysis magnet from an elastically scattered proton, and the Čerenkov counter veto only reduced the trigger rate by 1.6 in this case.

E. Backward spectrometer

The backward spectrometer, shown in Fig. 7, was on an axis 135° to the incident beam direction; this angle was determined by a Monte Carlo program to provide the largest geometrical acceptance for the given magnet aperture. Since the backward scattered pion kinematics are relatively independent of incident momentum in the range covered by this experiment, the same layout and spectrometer magnetic field could be used for all momenta, eliminating many instrumental uncertainties.

MWPC's were used to define particle trajectories on either side of the analysis magnet. Upstream of the magnet, horizontal track position was determined by two planes of vertical wires with 2 mm spacing, separated by 13 cm; vertical position by three planes of horizontal wires also with 2 mm spacing and separated by 13 and 10 cm. The chambers were aligned and fixed in a cradle attached to the front face of the magnet; this compact configuration permitted close placement of the analysis magnet to the target in order to maximize acceptance. The analysis-magnet aperture was 183 cm$\times$46 cm with a pole length of 46 cm; its central field was 4.2 kG with an effective field integral of 126 kG in. The magnetic-field polarity depended on incoming pion polarity and was such that the backward elastically scattered pion was always bent away from the incident beam. An incident beam channel

in the magnet return iron allowed the magnet to be positioned to maximize the pion scattering angle acceptance. The field in this channel introduced a slight deflection in the incident beam direction which was measured during calibration runs and corrected in the analysis. Behind the magnet, only the horizontal track projection was measured, using two planes of vertical wires. Wire spacing in the planes was 2 mm with adjacent wires joined together, yielding an effective spacing of 4 mm. The distance between planes was ~ 40 cm. To accommodate the large angular range of the backward scattered pions in the laboratory, these planes each consisted of several individual chambers positioned side by side; two in the first plane, three in the second. The chamber frames were overlapped to minimize holes in the acceptance. Monte Carlo calculation showed this effect to be smeared in u due to the finite target length and the acceptance was corrected accordingly. The sensitive areas of all wire planes were sufficiently large that they were not aperture limits.

Located behind the final MWPC plane was a hodoscope (S_1—S_{12} in Figs. 5 and 7). It consisted of 24 scintillation counters 11 in. wide$\times$12 in. high in a 2 high by 12 wide array. The pion position measured by this hodoscope gave approximate information on the pion momentum and scattering angle (assuming it to be elastic). This information was then used with that from the forward spectrometer telescopes in making the trigger decision. A single counter near the target (S_0 in Fig. 7) was put in coincidence with most of the S counters to help eliminate background triggers from particles not coming from the hydrogen target. The time between beam arrival and the signal in a particular hodoscope element was measured using time-to-digital converters (TDC's) and recorded for each event. This information proved useful in the off-line analysis in eliminating those remaining accidental triggers not originating in the target.

F. Fast logic

The fast-logic system rapidly identified events where the trajectories of both particles from the hydrogen target were consistent with those expected for an elastic event. A simplified block diagram is given in Fig. 8.

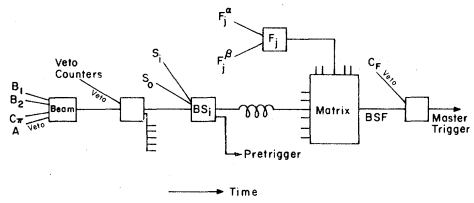

FIG. 8. Simplified fast-logic system.

A beam pion was identified by the coincidence $B = B_1 B_2 \bar{A} C_\pi$. To minimize background in the MWPC's, a beam pion was accepted only if it was not accompanied by a second beam particle within ± 25 nsec. A signal from an element of the S hodoscope at the correct time following B_2, defined as $BS = B \cdot S_0 \cdot (S_1 + S_2 + \cdots + S_{12})$, indicated that a particle had emerged from the target and passed through the backward arm. (S_0 was only used for channels S_3—S_{12}.) The BS signal was used as a pretrigger which temporarily disabled the experiment and stored the MWPC and S-hodoscope information in latches until the signals from the forward hodoscopes and Čerenkov counter were received and processed. Typically 1 beam pion in 2000 resulted in a BS pretrigger. The individual coincidences $BS_0 S_i$ were also formed and sent to delay lines for later use in forming the final trigger.

Following a delay of ~ 400 nsec, the forward-hodoscope signals were received and the coincidences $F_i = F_i^\alpha \cdot F_i^\beta$ ($i = 1,8$) were formed. At this point, the kinematic constraints were imposed. The signal BSF, defined as

$$BSF = \sum BS_i A_{ij} F_j, \quad i = 1,12, \quad j = 1,8 ,$$

where A_{ij} is an 8×12 matrix of 0's and 1's, was formed in a hard-wired coincidence matrix using commercial fan-ins, fan-outs, and coincidence circuits. This matrix contained all of the correlations between elements of the forward and backward hodoscopes for backward elastic events; the correlations were determined by Monte Carlo simulation of elastic events in the apparatus, and changed with incident momentum. A BSF signal thus indicated that an event had a hodoscope hit pattern consistent with that expected for an elastic event, although such patterns could also occur from inelastic scatters whose kinematics were close to elastic, and from interactions occurring upstream of the liquid hydrogen target. The latter source was dominant.

The final coincidence, master trigger$= BSF \cdot \bar{C}_F$, ensured that the forward particle was a proton. This caused a readout cycle transferring the event

TABLE III. Typical rates during the experiment.

Beam pions per accelerator cycle	1.5×10^6
BS pretriggers per accelerator cycle	750
Master triggers per accelerator cycle	10
Elastic events per accelerator cycle	(2×10^{-4})—(8×10^{-3})

data stored in the latches, TDC's, and scalers to the computer memory and eventually to magnetic tape. Upon completion of the transfer, the TDC's, latches, and appropriate scalers were reset and the experiment restarted. An entire event cycle took approximately 10 msec.

Any *BS* pretrigger which was not followed by the appropriate signals from the forward counters resulted in the clearing of all temporarily stored data and the prompt reenabling of the experiment without computer readout. The dead time thus introduced was ≤ 2 μsec. Approximately 99% of the pretriggers fell into this category. Table III gives some typical rates during the experiment.

A random selection of events triggered by beam only, and also by *BS* only, was recorded continuously throughout the data taking. The total number of pions, as defined by the beam telescope, incident on the liquid hydrogen target during the time the experiment was enabled was scaled at each momentum and used to normalize the final differential cross sections.

G. MWPC's

The MWPC's were each constructed of two sets of wire planes built on aluminum-reinforced G10 frames. Anode (signal) wires were 0.025-mm gold-plated tungsten, and cathode wires were 0.076-mm silver-clad beryllium-copper. The gap between anode and cathode was 5.4 mm. The gas was a mixture of 80% argon, 19.9% CO_2, and 0.1% freon 13B1. Typical operating voltages were 4—4.5 kV.

The readout system was based upon the Nevis Laboratory design of Sippach[28] and used amplifier/discriminator cards mounted on the MWPC's feeding long stripline delay cables. These cables in turn fed into coincidence registers (located in the experiment counting area) which were gated by signals from the fast logic. The MWPC's contained a total of 4300 wires.

III. DATA ANALYSIS

A. Introduction

The data from the experiment were analyzed on the Fermilab CDC-6600 computers. The analysis procedure for each event included the geometrical reconstruction, during which many obviously nonelastic events were excluded, followed by the calculation of several kinematic variables which were a measure of how near to elastic the event was. Elastic events were finally selected by making the appropriate cuts on these kinematic variables. Since the cross sections (and hence statistics) were small, particular attention was given to making the analysis program as efficient as possible in extracting elastic events from the data.

B. Reconstruction

The first stage of the analysis began with the geometrical reconstruction in the backward spectrometer. Tracks were first reconstructed in the horizontal (x) projection in front of and behind the analysis magnet. For this to be possible, at least three of the four MWPC x planes in the backward arm had to record at least one hit. From the measured efficiencies of the chambers, $>95\%$ of the pions from elastic interactions had trajectories which could be reconstructed. Events were divided into two groups: those in which all four x planes recorded at least one hit, and those in which only three of four x planes recorded hits.

For events in the first group, a track was formed by joining with a straight line a hit in one x plane with a hit in the other on the same side of the analysis magnet; if planes had more than one hit, all combinations were used to produce a set of tracks. This procedure was used to reconstruct tracks on both sides of the analysis magnet. To reduce the number of tracks which did not correspond to true charged-particle trajectories, a track behind the analysis magnet was accepted only if it extrapolated to an *S*-hodoscope element which had recorded a hit. If no track was accepted, it was assumed that one of the planes failed to record a true hit but contained spurious accidental hits. The event was then reclassified into the second group.

For events with only two hits on one side of the magnet and one on the other, tracks from the two-hit side were traced through the magnetic field to the hit on the opposite side by varying the curvature (momentum) of the track in the field region. All possible combinations were tried and again only those tracks behind the magnet which extrapolated to an *S*-hodoscope element which was hit were considered valid.

Either procedure described above produced two sets of tracks, one before and one after the magnet. Tracks from each set were paired with the requirement that they meet within the magnet volume, and the momentum was calculated. The event was required to have a track that pointed back to the liquid hydrogen target, and had the correct sign momentum. The TDC information was used to ensure that it had the proper time of flight from the target to the *S* hodoscope for an elastic pion.

Tracks were reconstructed in the vertical (y) projection before the magnet, with the requirement of hits in at least two of the three chambers. Events meeting all of the criteria described so far were

recorded on a data summary tape for further analysis. This first stage analysis eliminated ~90% of the raw triggers.

In the second stage of the analysis, incident beam tracks and tracks in the forward spectrometer were reconstructed in both x and y projections. For the beam tracks, information from both beam chambers was used unless there was no $W1$ chamber hit due to inefficiency. In the latter case position information from the $W2$ chamber was used and the nominal beam direction was assigned to the track. Due to the small divergence of the beam, this procedure introduced negligible error. A hit in $W2$ was always required. Each beam track was extrapolated through the channel in the backward-spectrometer magnet, taking into account the fringe field in the channel. It was then paired with a reconstructed track from the backward spectrometer, and the target-vertex coordinates as well as the x and y projections of the backward-pion scattering angle were calculated.

For the forward arm upstream of the analysis magnet, tracks in the x projection were reconstructed using $W4$ and the target vertex. $W3$ was not required but was included in the fit if it had a hit. In the event that there was no hit in $W4$, the track was constructed using a hit in $W5$ and extrapolating back through the magnet to the target vertex assuming the scattering to be elastic. Thus, the existence of a valid forward track and the horizontal projection of the proton scattering angle, θ_x^p, were determined by requiring only a hit either $W4$ or $W5$. The vertical projection of the angle, θ_y^p, was calculated using the target vertex and either $W4$ or $W3$. This procedure for determining the proton scattering angle minimized the number of events lost because of possible chamber inefficiencies. A kinematics program used the incident pion momentum and the backward scattering angle θ^π to predict the momenta of the backward pion and forward proton, P'_π and P'_p. The proton trajectory downstream of the analysis magnet was calculated using P'_p and the reconstructed proton track between the target and the analysis magnet. The event was rejected if the trajectory did not intersect the hodoscope elements in F^α and F^β which were involved in the trigger.

In anticipation of cuts which would be applied later, the variables x_π, ΔP_x, ΔP_y, and Δx_{W6} were calculated and recorded during the second stage of analysis. The first quantity is defined as

$$x_\pi = \frac{P_\pi - P'_\pi}{P_\pi \cdot P'_\pi}$$

and measures the discrepancy between the measured and predicted scattered pion momentum. It has the property that the width of the distribution of elastic events in x_π is constant for all scattered pion momenta, allowing the final elastic cut on this variable to be the same for all scattering angles. The second and third quantities are transverse-momentum imbalances defined by

$$\Delta P_{x,y} = P^\pi_{x,y} - P^p_{x,y} ,$$

where $P^\pi_{x,y} = P'_\pi \sin\theta^\pi_{x,y}$ and $P^p_{x,y} = P'_p \sin\theta^p_{x,y}$. The fourth quantity Δx_{W6} is the distance between the predicted intersection of a proton trajectory with $W6$ and the closest recorded hit in $W6$.

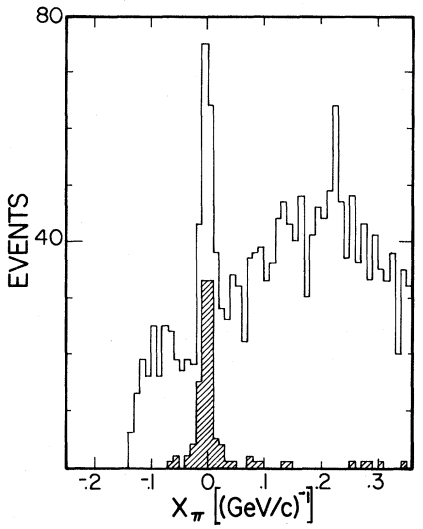

FIG. 9. Number of events as a function of x_π for 50-GeV/c $\pi^- p$ data. The shaded histogram shows the number of events after cuts on ΔP_x, ΔP_y, and Δx_{W6}.

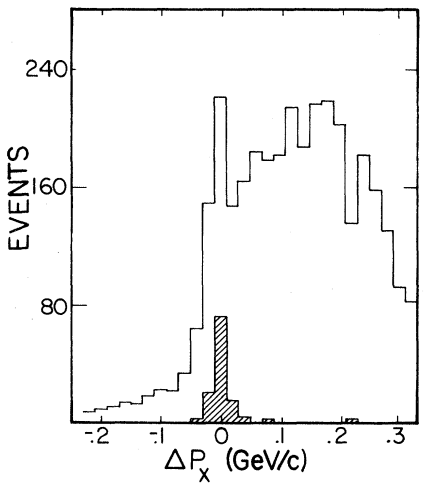

FIG. 10. Number of events as a function of ΔP_x for 50-GeV/c $\pi^- p$ data. The shaded histogram shows the number of events after cuts on x_π, ΔP_y, and Δx_{W6}.

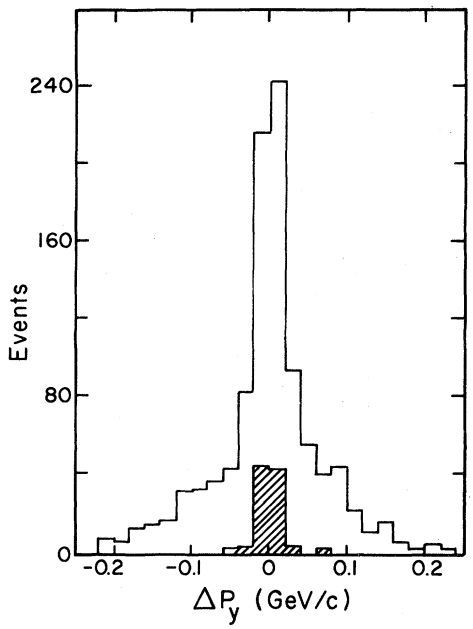

FIG. 11. Number of events as a function of ΔP_y for 50-GeV/c $\pi^- p$ data. The shaded histogram shows the number of events after cuts on x_π, ΔP_x, and Δx_{W6}.

C. Event selection

After the events were reconstructed, histograms were made of the number of events versus the variables x_π, ΔP_x, ΔP_y, and Δx_{W6}. Examples are shown in Figs. 9—12. In these figures, the unshaded histograms show the number of events before any kinematic cuts were applied. These plots all showed the same characteristic feature of a sharp peak about the (expected) value zero, containing the elastic events, superimposed on a rather smooth background of inelastic events. In the histogram of x_π, shown in Fig. 9, the inelastic background, as expected, is mostly to one side of the peak, since the momentum of an inelastically scattered pion is always less than that of an elastically scattered pion at the same angle. The width of the peak directly reflects the momentum resolution of the backward spectrometer.

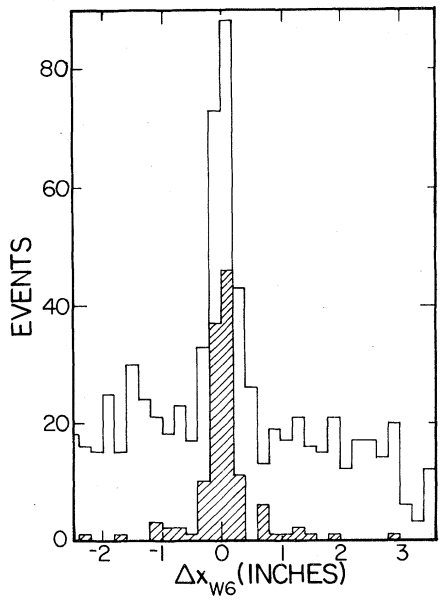

FIG. 12. Number of events as a function of Δx_{W6} for 50-GeV/c $\pi^- p$ data. The shaded histogram shows the number of events after cuts on x_π, ΔP_x, and ΔP_y.

The final selection of elastic events was made by choosing those events which fell within a prescribed interval about the elastic peak in each of the four variables. The limits of this interval for a given variable were determined by observing the width of the elastic peak in the variable after all of the other cuts were made. The shaded histograms in Figs. 9—12 show the number of events remaining after the cuts on all variables except the one plotted.

The events accepted by the elastic cuts were used to generate a final histogram of the number of events versus u, with the value of u for each event calculated from the scattering angle of the backward pion. Events in this histogram consisted of the true elastic scatters together with a small background of inelastic events under the elastic peak.

D. Inelastic background

Inelastic background in the final data sample was calculated using the distribution of events in the variable x_π. From a histogram similar to the lower curve of Fig. 9 (the distribution of events surviving the elastic cuts on all the variables except x_π), the background outside the elastic peak was found to be approximately flat for positive x_π, and to eventually fall to zero for negative x_π. To determine the amount of background beneath the elastic peak, the assumption was made that it varied linearly from its level on one side of the elastic peak to its level on the other. A $\pm 50\%$ systematic error in the background was included to allow for uncertainty in this procedure. The distribution of inelastic events in u was then determined by histogramming the u values of events which satisfied the elastic cuts on all variables except x_π. Assuming the inelastic events beneath the elastic peak had a similar distribution in u, a subtraction of the background could then be made. Since the statistics in this histogram were generally poor, fluctuations of the background level in u were smoothed out using a simple fit. Some checks of these procedures were made by selecting inelastic events from outside the elastic peak.

Within limited statistics, they were shown to be correct.

For the π^- data, the background subtraction was always less than 10% at 30, 50, and 70 GeV/c, but increased to $\sim 25\%$ at 90 GeV/c for $-u \geq 0.25$ (GeV/c)^2. For π^+, at 30 and 50 GeV/c and near $u=0$ for 70 GeV/c, the subtraction again never exceeded 10%. However, at 70 GeV/c, in the region of the dip and beyond [$-u \geq 0.5$ (GeV/c)^2] the background became equal to the signal. In this region, only upper limits are quoted for the cross section.

Quasi-two-body reactions such as $\pi p \to N^* \pi$, $N^* \to p\pi^0$ and $\pi p \to p\rho$, $\rho \to \pi\pi^0$ may not be correctly subtracted by the process described above. However, a Monte Carlo study showed that under 1% of such reactions would have decay charged particles falling within our analysis cuts. Around 10 GeV/c, these reactions have cross sections similar to elastic scattering,[29,30] and since they are also baryon-exchange processes, we would expect this to be also true for momenta between 30 and 90 GeV/c. They should therefore contribute a negligible background to our data.

E. Corrections and acceptance

The measured cross sections were corrected for muons and electrons in the pion beam (1.5—12.7%); more than one beam particle in a rf "bucket" (2%); absorption in the hydrogen target, air, Čerenkov-counter mirrors, MWPC's, and counters ($\sim 30\%$); and accidental vetos of elastic events by delta rays produced in the target (4.9%).

The geometrical acceptance of the apparatus at each incident momentum was determined by a Monte Carlo program. Elastic events were generated in the hydrogen target and the scattered particles propagated through the spectrometer arms with multiple scattering included; measured incident beam parameters (momentum spread, divergence, and spot size) were used. The probability of detecting an event was calculated as a function of u. The 30-GeV/c acceptance curve is shown in Fig. 13; curves for the other incident momenta are similar. Because the overall acceptance was essentially determined by the fixed vertical acceptance of the S-hodoscope counters, the acceptance curve exhibits an approximate $(\sin\theta^{\pi}_{\rm lab})^{-1}$ dependence expected for this type of geometrical constraint.

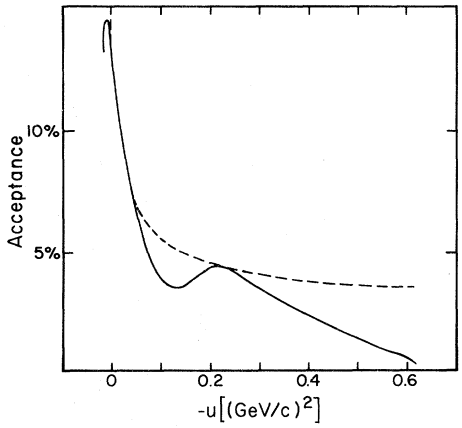

FIG. 13. Apparatus acceptance for 30-GeV/c data. Also shown as a dashed curve is a $(\sin\theta^{\pi}_{\rm lab})^{-1}$ curve which is the expected acceptance for a fixed vertical aperture at the S_1—S_{12} hodoscope.

MWPC efficiencies, measured during special calibration runs at various times during the data taking, varied between 85 and 98% depending on the chamber. Chamber response as a function of time was very stable.

The efficiency of the analysis program for identifying elastic events as a function of u was measured using Monte Carlo generated events. Included in the event generating procedure were the effects of MWPC spatial resolution, MWPC efficiency, multiple Coulomb scattering, incident beam phase space, and scattered pion decay. To account for the effect of the additional random background hits present in the MWPC's and hodoscopes, real data taken at random times during the beam spill were added to the Monte Carlo generated elastic MWPC and hodoscope data. The resulting events were then processed by the analysis program. Including the effects mentioned above, between 78 and 86% of the elastic events were identified as such. Most of the events that were not identified as elastic lacked sufficient MWPC data due to the measured chamber efficiencies included in the program. If the chambers had been 100% efficient, the program would have identified $>98\%$ of the Monte Carlo events as being elastic.

Radiative corrections were calculated using the procedure outlined in Refs. 31—34. For $\pi^+ p$ scattering, the correction was negligible; for $\pi^- p$ the correction changed the overall normalization of the differential cross sections by a factor 1.14—1.18 depending on momentum. The correction was independent of scattering angle.

Several runs were taken with the target empty to determine the contribution from events not originating in the liquid hydrogen. It was found to be negligible.

IV. RESULTS

The results are presented in tabular form in Tables IV and V, and graphically in Figs. 14 and 15 (together with some earlier results). The errors quoted are statistical and represent 1 standard devia-

TABLE IV. Differential cross sections, $\pi^- p \to p\pi^-$. Statistical errors only are listed; there is an additional overall normalization uncertainty of ±15%.

Incident momentum (GeV/c)	u [(GeV/c)^2]	Δu [(GeV/c)^2]	$d\sigma/du$ [nb/(GeV/c)^2]
30.0	+0.004	0.008	225.2±53.1
	−0.010	0.020	172.5±33.2
	−0.035	0.030	125.4±27.4
	−0.070	0.040	124.2±29.3
	−0.110	0.040	111.2±30.9
	−0.155	0.050	85.0±24.5
	−0.210	0.060	86.9±22.4
	−0.285	0.090	53.6±15.5
	−0.380	0.100	33.2±13.6
	−0.480	0.100	<23.4
50.0	−0.004	0.013	55.8±13.6
	−0.025	0.030	62.7±11.4
	−0.060	0.040	60.0±11.2
	−0.105	0.050	49.9±11.8
	−0.160	0.060	30.2± 8.6
	−0.240	0.100	10.7± 4.3
	−0.340	0.100	6.0± 3.5
	−0.440	0.100	3.1± 3.1
70.0	−0.013	0.024	20.8± 7.4
	−0.100	0.150	15.8± 4.1
	−0.250	0.150	8.1± 3.3
	−0.400	0.150	<5.5
90.0	−0.014	0.023	15.2± 7.6
	−0.100	0.150	9.4± 3.9
	−0.250	0.150	5.1± 3.8
	−0.400	0.150	<7.8

tion. For those bins in which no signal above background was found, the cross sections are given as upper limits and represent 90% confidence levels. Because of uncertainties in the previously discussed corrections, the uncertainty in the overall normalization of the cross sections is estimated to be ±15%.

A. General features

(1) The u distributions of the cross sections $d\sigma/du$ for both π^+ and π^- we have measured at 30 GeV/c and above are similar to those previously obtained below 20 GeV/c. In Figs. 14 and 15, the results may be compared with the π^+ results of Baker *et al.*[8] at 7 GeV/c and the π^- results of Owen *et al.*[7] at 6 GeV/c. For $\pi^+ p$ scattering the steep backward peak and the dip at $-u=0.15$ (GeV/c)^2 as well as the broad second maximum between $-u=0.15$ and 0.45 (GeV/c)^2 are all present, at least up to 50 GeV/c. The data at 70 GeV/c are also consistent with these features.

(2) In the region of the backward peak, the cross section has an approximately exponential dependence on u. The data in the region $-u \lesssim 0.1$ (GeV/c)^2 for positive-pion scattering and $-u \lesssim 0.5$ (GeV/c)^2 for negative-pion scattering were fit using the relation $d\sigma/du = Ae^{Bu}$. The fitted values for A and B are given in Table VI. The values of B range from 21 to 26 (GeV/c)$^{-2}$ for positive-pion scattering and from 4 to 7 (GeV/c)$^{-2}$ for negative-pion scattering. These are compared with the values of B obtained at lower momenta in Fig. 16. For both polarities, they are consistent with a slow increase in B for incident momenta between 5 and 90 GeV/c.

(3) The cross section $d\sigma/du$ at $u=0$ for $\pi^+ p$ is greater than for $\pi^- p$ at all measured momenta. The ratio of $\pi^+ p/\pi^- p$ is 1.9±0.3 at 30 GeV/c, 1.3±0.3 at 50 GeV/c, and 1.5±0.8 at 70 GeV/c.

(4)The cross section $d\sigma/du$ at $u=0$, for both positive and negative pions, decreases with increasing momentum. The available data above 5 GeV/c including our own have been fit to the form

TABLE V. Differential cross sections, $\pi^+p \to p\pi^+$. Statistical errors only are listed; there is an additional overall normalization uncertainty of ±15%.

Incident momentum (GeV/c)	u [(GeV/c)^2]	Δu [(GeV/c)^2]	$d\sigma/du$ [nb/(GeV/c)^2]
30.0	+0.003	0.011	351.1±62.6
	−0.011	0.018	270.4±51.1
	−0.030	0.020	176.9±43.5
	−0.075	0.070	66.4±17.1
	−0.115	0.090	<12.3
	−0.250	0.100	18.6± 9.3
	−0.350	0.100	54.1±19.1
	−0.450	0.100	56.5±23.1
	−0.550	0.100	17.4±17.4
50.0	0.000	0.008	96.9±25.9
	−0.014	0.020	65.2±15.8
	−0.042	0.036	40.4±11.2
	−0.080	0.040	11.8± 6.8
	−0.135	0.070	5.8± 4.1
	−0.215	0.090	11.8± 5.3
	−0.305	0.090	12.1± 5.6
	−0.400	0.100	10.9± 6.3
	−0.500	0.100	6.0± 6.0
70.0	−0.011	0.018	26.6± 9.7
	−0.045	0.050	12.2± 5.1
	−0.120	0.100	<4.4
	−0.245	0.150	<3.3
	−0.395	0.150	<6.3

$$\frac{d\sigma}{du}(P,u=0)=KP^{-n}.$$

For the fits, the quoted statistical and systematic errors were added in quadrature for each experiment. For π^+, the data from Babaev *et al.*[22] at 23 and 38 GeV/c were not included in the fits (for reasons explained below). The results are shown in Fig. 17. We obtain the values $n^+=2.31\pm0.07$ and $n^-=2.08\pm0.06$ with χ^2 probabilities of 26% and 21%, respectively. Fits to the data of this experiment only yield the values $n^+=2.51\pm0.36$ and $n^-=2.11\pm0.21$. Within errors, the two sets of results are consistent.

(5) The data do not confirm the large values of $d\sigma/du$ at $u=0$ for π^+p scattering, nor the large values of the π^-p slope parameter B observed in the data of Babaev *et al.*[22,23] As shown in Fig. 17, their 40-GeV/c π^+p result is approximately 2.5 times larger than that expected from a smooth interpolation between the measurements of this experiment at 30 and 50 GeV/c. The angular distributions however are quite similar (see Fig. 15). For π^-p scattering, the two experiments observe substantially different angular distributions as shown in Fig. 14, where the 38-GeV/c Babaev *et al.*[23] results have been included for comparison. Fits by Babaev *et al.* to their data yield values for the parameter B of 23 and 19 (GeV/c)$^{-2}$ at 25 and 38 GeV/c, respectively, in comparison to the values of B between 4 and 7 (GeV/c)$^{-2}$ for this experiment (see Fig. 16). It should be pointed out that their data covered a much narrower u range than ours, hence their fits were limited to the region very close to $u=0$. The possibility that a real physics effect near $u=0$ leads to a sharp peak in the π^- distribution cannot entirely be ruled out. However our data, particularly at 50 GeV/c, do not support this hypothesis. Statistically, the Babaev *et al.* values of B are ~2–2.5 standard deviations from the values expected by interpolation from other data, as seen in Fig. 16.

B. Discussion

As was mentioned in the Introduction, many of the features of both π^+p and π^-p backward elastic scattering between the resonance region and 20 GeV/c can be explained by a simple Reggeized baryon-exchange model using only the N_α and Δ_δ trajectories. We find the same to be true for the

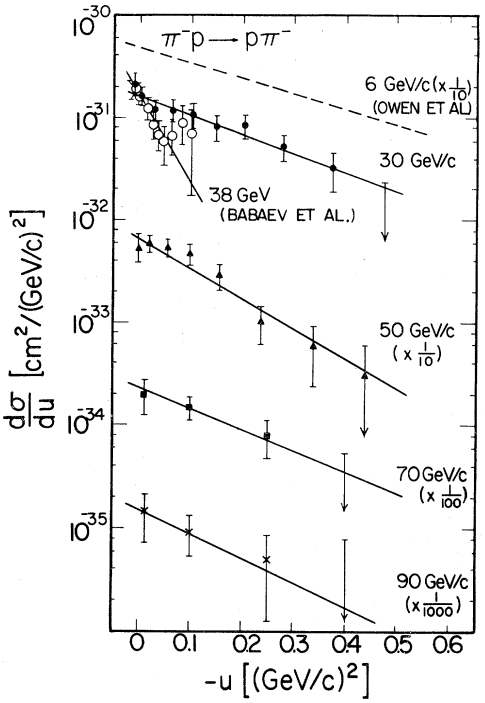

FIG. 14. Results of this experiment for the u dependence of $d\sigma/du$ for $\pi^- p$ backward elastic scattering; upper error limits are 90% confidence. Solid lines are fits of the form Ae^{Bu} to the present data and those of Babaev *et al.* (Ref. 23). Results of Owen *et al.* (Ref. 7) are represented by a dashed line.

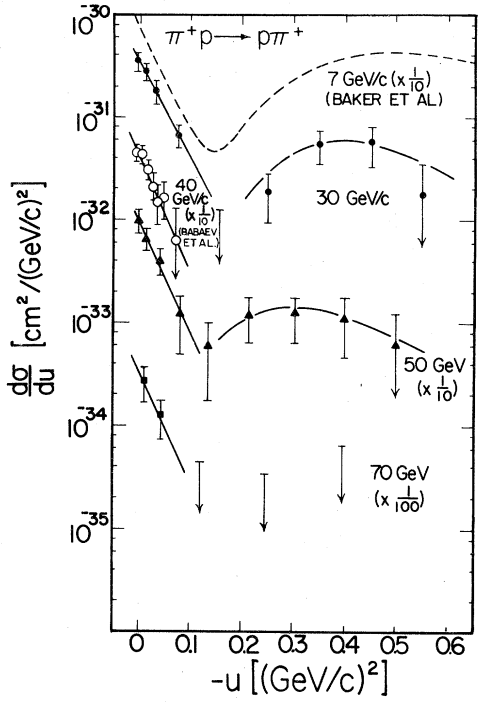

FIG. 15. Results of this experiment for the u dependence of $d\sigma/du$ for $\pi^+ p$ backward elastic scattering; upper error limits are 90% confidence. Solid lines are fits of the form Ae^{Bu} to the present data and those of Babaev *et al.* (Ref. 22). Results of Baker *et al.* (Ref. 8) are represented by a dashed curve. Remaining curves are to guide the eye.

data obtained by this experiment between 30 and 90 GeV/c. In the model, the dip in the $\pi^+ p$ differential cross section at $-u \simeq 0.15$ (GeV/c)^2 occurs because the amplitude of the N_α trajectory, assumed to dominate this process, vanishes at this u value. Since in $\pi^- p$ scattering, the exchange of the nucleon trajectory cannot occur, a dip is neither expected nor seen at this u value.

The model also predicts the width of the backward peaks to slowly decrease with increasing momentum. Since experimentally the backward peaks at all energies may be parametrized by the form Ae^{Bu}, the parameter B should increase with increasing momentum P as $B \simeq 2\ln(P) + \text{constant}$. The data above 5 GeV/$c$ including those of this experiment, as shown in Fig. 16, are consistent with this form.

The Regge model prediction that the cross section $d\sigma/du$ for any value of u varies with increasing momentum as $s^{2\alpha(u)-2}$, where s is the c.m.s. energy squared and $\alpha(u)$ is the trajectory of the exchanged Reggeon, can be used to derive effective Regge trajectories. These can be compared with the Δ_δ and the N_α trajectories which are assumed to dominate π^- and π^+ scattering, respectively, as a check of the validity of this simple model. The available π^- and π^+ backward elastic data above 5 GeV/c including those of this experiment (and also the data of this experiment alone) have been fitted using this parametrization for several values of u in the range $0 < -u < 0.5$ (GeV/c)^2. The χ^2 probabilities of the fits, which vary from 50% to 5% and from 70% to 10% as $-u$ increases from 0 to 0.5 (GeV/c)^2 for π^+ and π^- scattering, respectively, are an indication that this parametrization describes the data well. In

TABLE VI. Exponential fit of backward peaks.

Incident momentum (GeV/c)	A [nb/(GeVc)^2]	B [(GeV/c)$^{-2}$]
+30.0	333.8±43.4	21.4± 3.8
+50.0	96.7±18.9	24.3± 6.0
+70.0	36.8±15.7	26.3±13.1
−30.0	175.0±20.0	4.37± 0.78
−50.0	73.2± 8.8	6.89± 0.92
−70.0	24.1± 6.6	4.71± 1.97
−90.0	16.1± 7.5	5.07± 4.01

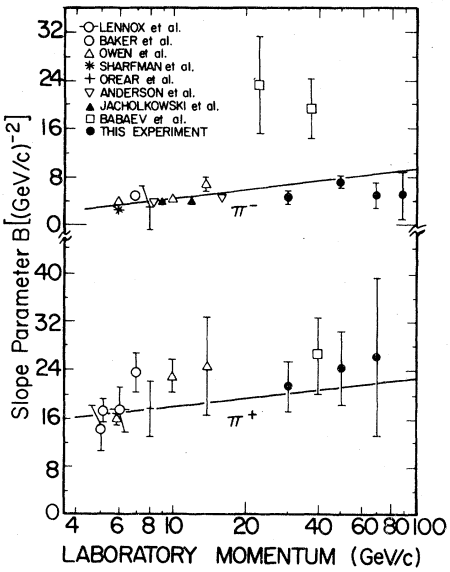

FIG. 16. Results for B. Data are shown from this experiment and from Refs. 4, 6–10, 12, 22, and 23. The two lines shown are fits, of the form $B=2\ln(P)+$ a constant, to the data for each pion sign.

the fitting procedure, a 15% systematic error was added to the quoted statistical error of each experiment to allow for uncertainty in the absolute normalization of the different experiments. The results of the fits, expressed in terms of $\alpha(u)$, are shown in Figs. 18 and 19 for π^- and π^+ scattering, respectively.

For $\pi^- p$ scattering, a linear least squares fit to the effective trajectory gives

$$\alpha(u)=-(0.06\pm0.05)+(0.50\pm0.26)u$$

[where u is in (GeV/c)^2] for the 5–90-GeV/c data, and

$$\alpha(u)=-(0.11\pm0.14)+(0.67\pm1.04)u$$

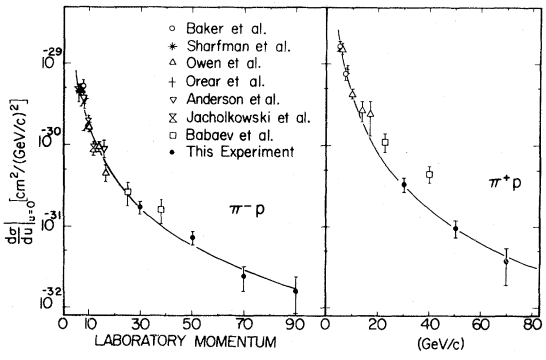

FIG. 17. Results for $d\sigma/du$ at $u=0$. Data are shown from this experiment and Refs. 4, 6–8, 10, 12, 22, and 23. The curves are the fits described in the text.

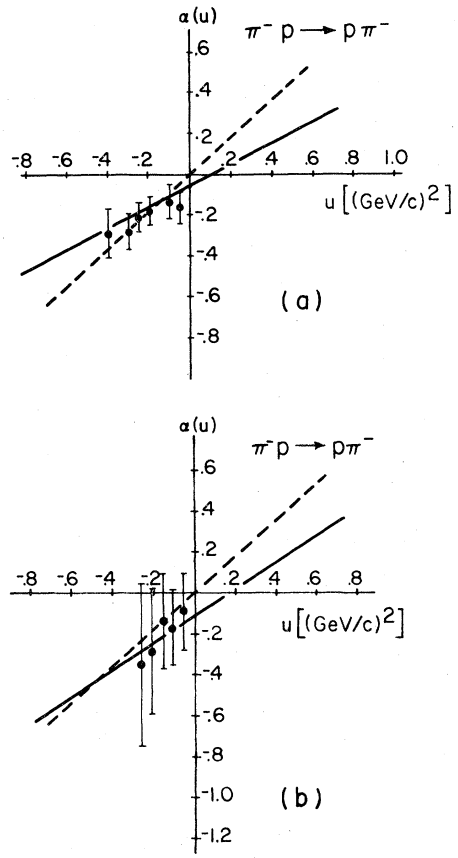

FIG. 18. The effective trajectory for $\pi^- p$ backward elastic scattering, derived as described in the text. The solid line is a linear fit to the data; the dashed line is the expected Δ_δ trajectory. (a) Data from this experiment and Refs. 4 and 6–8. (b) Data from this experiment only.

for fits to the 30–90-GeV/c data of this experiment only. These results are consistent with the form of the Δ_δ trajectory,

$$\alpha(u)=0.0+0.9u\ ,$$

obtained from Regge fits at lower energies.[18,19] The $u=0$ intercept of the effective trajectory gives the momentum dependence of the cross section $d\sigma/du$ at $u=0$ of $P^{2\alpha(0)-2}\sim P^{-2.12}$, close to the $P^{-2.0}$ predicted by the model.

For $\pi^+ p$ scattering, we find the linear fit to the effective trajectory of the 5–70-GeV/c data (omitting Ref. 22 as discussed earlier),

$$\alpha(u)=-(0.15\pm0.06)+(2.24\pm0.25)u\ ,$$

to be somewhat steeper in u than expected for the N_α trajectory, which from low-energy Regge fits is parametrized as[18,19]

$$\alpha(u)=-0.37+0.9u\ .$$

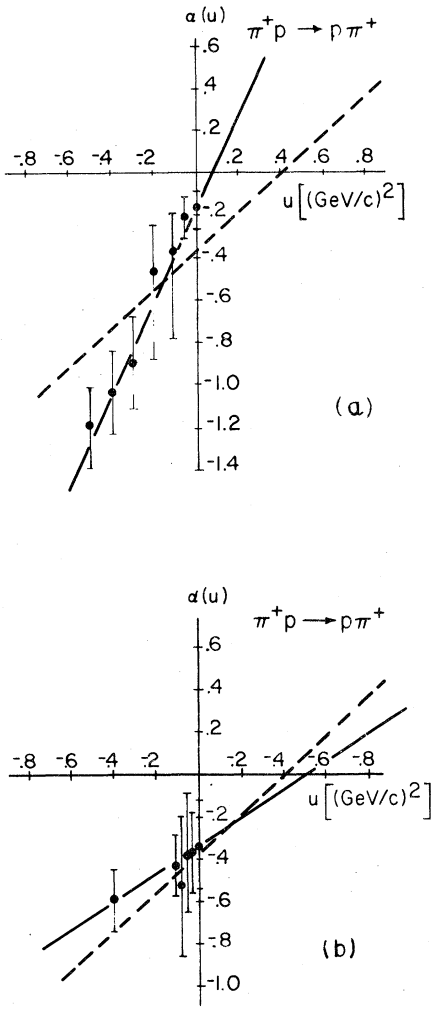

FIG. 19. The effective trajectory for π^+p backward elastic scattering, derived as described in the text. The solid line is a linear fit to the data; the dashed line is the expected N_α trajectory. (a) Data from this experiment and Refs. 4, 7, and 8. (b) Data from this experiment only.

However, we find the effective trajectory derived in the range 30–70 GeV/c from the data of this experiment only,

$$\alpha(u)=-(0.37\pm0.11)+(0.58\pm0.50)u\ ,$$

to be in better agreement. The higher $u=0$ intercept of the effective trajectory from the 5–70 GeV/c data, $\alpha(u)=-0.15$, gives a momentum dependence for $d\sigma/du$ at $u=0$ of $P^{-2.31}$ as opposed to the $P^{-2.7}$ dependence predicted by the model. If we use this $P^{-2.31}$ parametrization for extrapolation, the prediction for the momentum at which the π^- cross section becomes larger than π^+ becomes $\sim$400 GeV/c.

For both π^+ and π^-, the observed shapes of the u distributions are in reasonable agreement with predictions made several years ago from the simple

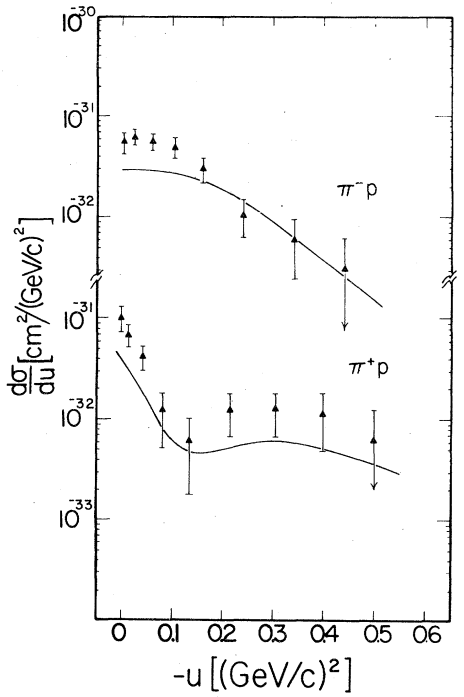

FIG. 20. Comparison between the 50-GeV/c $\pi^\pm p$ data from this experiment and the predictions of the simple Regge model discussed in Ref. 18 (solid curves).

Regge model[18]; this is illustrated in Fig. 20 for our 50-GeV/c data.

C. Phenomenological Regge-model fit

Since publication of our preliminary data,[2] an analysis of all backward scattering results including ours has been carried out by Mir and Storrow[35] based upon their earlier analyses using data up to 20 GeV/c.[19] In particular they examined the consistency of the lower momentum results upon which the predictions for higher momenta are based. They also included polarization data in their fitting.

As has been noted in the literature over the past several years, there are disagreements in the absolute normalizations quoted for the different experiments below 20 GeV/c. This leads to disagreements in the predictions for higher momenta, since the parameters of the model will vary according to which low momentum data are used.

Their model has three Regge exchanges, with the N_γ added to the two we have discussed earlier. The three trajectories are

$$N_\alpha:\ \alpha(u)=-0.37+0.90u\ ,$$

$$N_\gamma:\ \alpha(u)=-0.43+0.90u\ ,$$

$$\Delta_\delta:\ \alpha(u)=0.90u\ .$$

In addition, the Δ_δ trajectory is modified from the standard Regge model by allowing the real and imaginary parts to have separate parametrizations.

Mir and Storrow allow the relative normalizations of the lower-momentum experiments to float. In fitting to all of the data (both low momenta and ours), they find that normalization of lower momentum data to Anderson *et al.*[6] does not give good fits. There is a slight preference for normalization to Baker *et al.*[8] rather than to Owen *et al.*[7] and the χ^2 of the fits improve if the π^+ data of Owen *et al.* are omitted from the fits. Examples of their fits to our data, using the Baker *et al.*[8] normalization, are shown in Figs. 21 and 22, and it can be seen that this model provides good fits. The Babaev *et al.*[23] $\pi^- p$ data is not ruled out, although the large values of B they quote are 2–2.5 standard deviations above values consistent with all other data. The $\pi^- n \to \pi^- n$ data of Babaev *et al.*[22] are rejected as inconsistent with all other $\pi^+ p \to \pi^+ p$ data, as we have noted earlier.

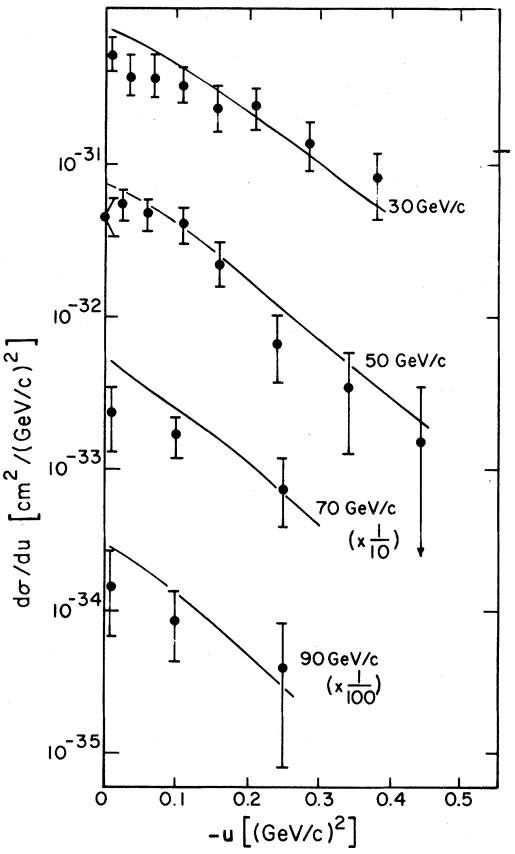

FIG. 21. Fits to the $\pi^- p$ data of this experiment by Mir and Storrow (Ref. 35) using their Regge model.

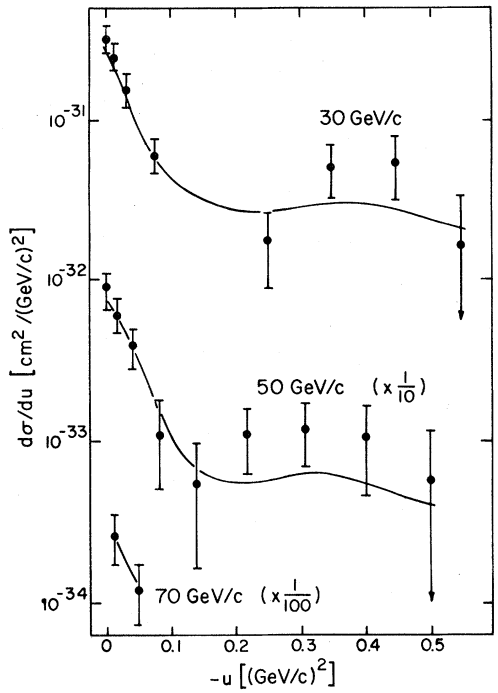

FIG. 22. Fits to the $\pi^+ p$ data of this experiment by Mir and Storrow (Ref. 35) using their Regge model.

V. CONCLUSIONS

We have measured $\pi^\pm p$ backward elastic scattering between 30 and 90 GeV/c. The data show that features of this process observed at lower momenta continue to be present in this new momentum range. Among the observations are the following.

(i) $d\sigma/du$ has an exponential shape near $u=0$ for both $\pi^+ p$ and $\pi^- p$.

(ii) $d\sigma/du$ at $u=0$ falls as P^{-n} for both $\pi^+ p$ and $\pi^- p$.

(iii) The dip in $d\sigma/du$ for $\pi^+ p$ at $-u \sim 0.15$ (GeV/c)^2 is still present at high momenta.

(iv) The data of Babaev *et al.* on $\pi^- n \to \pi^- n$ (isotopically equivalent to $\pi^+ p \to \pi^+ p$) at ~ 25 and 40 GeV/c are inconsistent with our data and all other $\pi^+ p$ data. Their values of the exponential slope for $\pi^- p$ scattering are 2–2.5 standard deviations higher than consistent with other data.

(v) Regge models are able to fit the new data. We have shown simple Regge fits to previous data and the new data presented here. We have commented on a more comprehensive analysis carried out which includes our data; while some (not unexpected) modifications have to be made to the simplest Regge ideas, in general the results provide support to the Regge model.

ACKNOWLEDGMENTS

We wish to thank C. Brown, E. Malamud, T. Toohig, and the Meson Department staff for their help; R. Cavanaugh, A. Cook, J. Upton, and H. Vaid for their technical assistance; and D. Kaplan for assistance in data taking. This work was supported by the U.S. Department of Energy and the National Science Foundation.

---

*Present address: Fairchild Republic, Farmingdale, New York 11735.

†Deceased.

‡Present address: Max-Planck Institute, Munich, Germany.

[1] u is the four-momentum transfer squared, given by the expression $u = u_{\max} - 2q^2(1+\cos\theta^{\pi}_{\text{c.m.s.}})$; $u_{\max} = (m_p{}^2 - m_\pi{}^2)^2/s$, s=(total c.m.s. energy)^2, q=c.m.s. momentum, $\theta^{\pi}_{\text{c.m.s.}}$=pion c.m.s. scattering angle.

[2] W. F. Baker, D. P. Eartly, R. M. Kalbach, J. S. Klinger, A. J. Lennox, P. A. Polakos, A. E. Pifer, and R. Rubinstein, Phys. Rev. Lett. 43, 1635 (1979).

[3] Aachen—Berlin—Birmingham—Bonn— Hamburg— London (Imperial College)—Munchen Collaboration, Phys. Lett. 10, 248 (1964).

[4] J. Orear, R. Rubinstein, D. B. Scarl, D. H. White, A. D. Krisch, W. R. Frisken, A. L. Read, and H. Ruderman, Phys. Rev. 152, 1162 (1966).

[5] H. Brody, R. Lanza, R. Marshall, J. Niederer, W. Selove, M. Shochet, and R. VanBerg, Phys. Rev. Lett. 16, 828 (1966); 16, 968(E) 1966.

[6] E. W. Anderson, E. J. Bleser, H. R. Blieden, G. B. Collins, D. Garelick, J. Menes, F. Turkot, D. Birnbaum, R. M. Edelstein, N. C. Hein, T. J. McMahon, J. Mucci, and J. Russ, Phys. Rev. Lett. 20, 1529 (1968).

[7] D. P. Owen, F. C. Peterson, J. Orear, A. L. Read, D. G. Ryan, D. H. White, A. Ashmore, C. J. S. Damerell, W. R. Frisken, and R. Rubinstein, Phys. Rev. 181, 1794 (1969).

[8] W. F. Baker, K. Berkelman, P. J. Carlson, G. P. Fisher, P. Fleury, D. Hartill, R. Kalbach, A. Lundby, S. Mukhin, R. Nierhaus, K. P. Pretzl, and J. Woulds, Nucl. Phys. B25, 385 (1971).

[9] A. J. Lennox, J. A. Poirier, C. A. Rey, O. R. Sander, W. F. Baker, D. P. Eartly, K. P. Pretzl, S. M. Pruss, A. A. Wehmann, and P. Koehler, Phys. Rev. D 11, 1777 (1975).

[10] A. Jacholkowski, B. Bouquet, B. D'Almagne, A. Ferrer, A. Lahellec, P. Petroff, F. Richard, P. Roudeau, J. Six, D. Treille, P. Rivet, P. Benkheiri, P. Fleury, G. De Rosny, A. Rouge, and H. Yoshida, Nucl. Phys. B126, 1 (1977).

[11] N. A. Stein, R. M. Edelstein, D. R. Green, H. J. Halpern, E. J. Makuchowski, J. S. Russ, D. M. Weintraub, Z. Bar-Yam, J. P. Dowd, W. Kern, J. J. Russell, N. Sharfman, and M. N. Singer, Phys. Rev. Lett. 39, 378 (1977).

[12] N. Sharfman, Z. Bar-Yam, J. R. Dowd, W. Kern, J. J. Russell, M. N. Singer, R. M. Edelstein, D. R. Green, H. J. Halpern, E. J. Makuchowski, J. S. Russ, and N. A. Stein, Phys. Rev. Lett. 40, 681 (1978).

[13] L. M. Simmons, Phys. Rev. Lett. 12, 229 (1964).

[14] M. Derrick, CERN Report No. 68-7, 1968 (unpublished), Vol. I, p. 111.

[15] C. B. Chiu and J. D. Stack, Phys. Rev. 153, 1575 (1967).

[16] V. Barger and D. Cline, Phys. Rev. Lett. 21, 392 (1968).

[17] V. Barger and D. Cline, Phys. Rev. 155, 1792 (1967).

[18] E. L. Berger and G. F. Fox, Nucl. Phys. B26, 1 (1971).

[19] J. K. Storrow and G. A. Winbow, Nucl. Phys. B53, 62 (1973); B54, 560 (1973); J. Phys. G 1, 263 (1975).

[20] A. C. Irving and R. P. Worden, Phys. Rep. 34, 117 (1977).

[21] E. Leader, Nature 271, 213 (1978).

[22] A. Babaev, E. Brakhman, G. Eliseev, A. Ermilov, Yu. Galaktionov, Yu. Gorodkov, V. Kirilyuk, N. Luzhetsky, V. Lyubimov, V. Nagovitzin, V. Nozik, V. Pogidaev, V. Shepelev, E. Shumilov, I. Sidorov, I. Tikhomirov, T. Tsvetkova, and O. Zeldovich, Phys. Lett. 38B, 342 (1972).

[23] A. Babaev, E. Brakhman, M. Danilov, G. Eliseev, A. Ermilov, Yu. Galaktionov, Yu. Gorodkov, L. Laptin, V. Lyubimov, V. Nagovitzin, V. Plyaskin, V. Shepelev, E. Shumilov, V. Sopov, I. Tikhomirov, T. Tsvetkova, and O. Zeldovich, Phys. Lett. 67B, 351 (1977).

[24] I. F. Ginzburg and L. I. Perlovskii, Yad. Fiz. 17, 1296 (1973) [Sov. J. Nucl. Phys. 17, 675 (1973)]; 23, 230 (1976) [23, 120 (1976)].

[25] B. Diu and P. Tchang, Nuovo Cimento 32A, 185 (1976).

[26] V. A. Lyubimov, Usp. Fiz. Nauk 123, 3 (1977) [Sov. Phys. Usp. 20, 691 (1977)].

[27] J. R. Orr and A. L. Read, Meson Laboratory preliminary design report, Fermilab, 1971 (unpublished).

[28] H. Cunitz, W. Sippach, and J. Dieperink, Nucl. Instrum. Methods 91, 211 (1971).

[29] A. Rouge, G. De Rosny, P. Fleury, B. Eisenstein, P. Briandet, P. Benkheiri, P. Rivet, A. Volte, B. Bouquet, B. D'Almagne, A. Ferrer, A. Jacholkowski, P. Petroff, F. Richard, P. Roudeau, J. Six, D. Treille, and H. Yoshida, Phys. Lett. 69B, 115 (1977).

[30] P. Benkheiri, B. Eisenstein, P. Fleury, G. De Rosny, A. Rouge, J. M. Thenard, H. Yoshida, D. Treille, P. Rivet, A. Volte, B. Bouquet, B. D'Almagne, A. Ferrer, A. Jacholkowski, P. Petroff, F. Richard, P. Roudeau, and

J. Six, Lett. Nuovo Cimento 20, 297 (1977).
[31]M. R. Sogard, Phys. Rev. D 9, 1486 (1974).
[32]E. Borie, Z. Naturforsch A 33, 1436 (1978).
[33]I. F. Ginzburg, G. L. Kotkin, and V. G. Serbo, Phys. Lett. 80B, 101 (1978).
[34]J. S. Klinger, Report No. Fermilab-Pub.-80/26-Exp, 1980 (unpublished).
[35]K. L. Mir and J. K. Storrow, J. Phys. G 7, 1187 (1981).